PAPER • OPEN ACCESS

Advances in physics and applications of 3D magnetic perturbations on the J-TEXT tokamak

To cite this article: Nengchao Wang *et al* 2022 *Nucl. Fusion* **62** 042016

OPEN ACCESS
IOP Publishing | International Atomic Energy Agency Nuclear Fusion
Nucl. Fusion **62** (2022) 042016 (14pp) https://doi.org/10.1088/1741-4326/ac3aff

Advances in physics and applications of 3D magnetic perturbations on the J-TEXT tokamak

Nengchao Wang[1,*], Y. Liang[1,2,3,*], Yonghua Ding[1], Zhongyong Chen[1], Zhipeng Chen[1], Zhoujun Yang[1], Donghui Xia[1], Wei Zheng[1], Wei Yan[1], Da Li[1], Zhonghe Jiang[1], Lu Wang[1], Bo Rao[1], Qiming Hu[4], Xiaolong Zhang[5], Junli Zhang[1], Xixuan Chen[1], Xin Xu[1], Tao Xu[1], Xianli Xie[1], Zhuo Huang[1], Feiyue Mao[1], Dongliang Han[1], Jianchao Li[6], Tong Wang[1], Linzi Liu[1,7], Ruihai Tong[1,7], Zhifang Lin[1,8], Yunong Wei[1], Nianheng Cai[1], Yuejiang Shi[9], Yaping Zhang[1], Weixin Guo[1], Xiaoqing Zhang[1], Peng Shi[10], Zhifeng Cheng[1], Ping Zhu[1], Minghai Liu[1], Shaoxiang Ma[1], Yong Yang[1], Chuan Li[1], Li Gao[1], Zhijiang Wang[1], Ming Zhang[1], Kexun Yu[1], Xiwei Hu[1], Q. Yu[11], K.W. Gentle[12], Yuan Pan[1] and the J-TEXT Team[a]

[1] International Joint Research Laboratory of Magnetic Confinement Fusion and Plasma Physics (IFPP), State Key Laboratory of Advanced Electromagnetic Engineering and Technology, School of Electrical and Electronic Engineering, Huazhong University of Science and Technology, Wuhan 430074, China
[2] Forschungszentrum Jülich GmbH, Institut für Energie- und Klimaforschung—Plasmaphysik, 52425 Jülich, Germany
[3] Institute of Plasma Physics, Chinese Academy of Sciences, Hefei 230031, China
[4] Princeton Plasma Physics Laboratory, PO Box 451, Princeton, NJ 08543, United States of America
[5] Advanced Energy Research Center, Shenzhen University, Shenzhen 518060, China
[6] Hubei Key Laboratory of Optical Information and Pattern Recognition, Wuhan Institute of Technology, Wuhan, 430205, China
[7] Southwestern Institute of Physics, Chengdu 610041, China
[8] Jiangsu Normal University, School of Electrical Engineering & Automation, Xuzhou 221116, China
[9] Hebei Key Laboratory of Compact Fusion, Langfang 065001, China
[10] United Kingdom Atomic Energy Authority (CCFE), Culham Science Centre, Abingdon, Oxon, OX14 3DB, United Kingdom of Great Britain and Northern Ireland
[11] Max-Planck-Institut für Plasmaphysik, D-85748 Garching, Germany
[12] Institute of Fusion Studies, University of Texas at Austin, Austin, TX 78712, United States of America

E-mail: wangnc@hust.edu.cn and y.liang@fz-juelich.de

Received 30 May 2021, revised 20 October 2021
Accepted for publication 18 November 2021
Published 21 March 2022

Abstract

In the last two years, three major technical improvements have been made on J-TEXT in supporting of the expanded operation regions and diagnostic capabilities. (1) The successful commission of the 105 GHz/500 kW/1 s electron cyclotron resonance heating (ECRH) system increasing the core electron temperature from 0.9 keV up to around 1.5 keV. (2) The poloidal divertor configuration with an *X*-point in the high-field side has been achieved. In particular,

[*] Authors to whom any correspondence should be addressed.
[a] See appendix.

the 400 kW electron cyclotron wave has also been successfully injected into the diverted plasma. (3) A 256-channel electron cyclotron emission imaging diagnostic system and two sets of four-channel Doppler backscattering diagnostics have been successfully developed on J-TEXT, allowing detailed measurement of the electron temperature and density fluctuations for turbulence and MHD research. The locked mode (LM), especially the 2/1 LM, is one of the biggest threats to the plasma operation. Both the thresholds of 2/1 and 3/1 LM are observed to vary non-monotonically on electron density. The electrode biasing was applied successfully to unlock the LM from either a rotating or static resonant magnetic perturbation (RMP) field. In the presence of 2/1 LM, three kinds of standing wave (SW) structures have been observed to share a similar connection to the island structure, i.e. the nodes of the SWs locate around the *O*- or *X*-points of the 2/1 island. The control and mitigation of disruption is essential to the safe operation of ITER, and it has been systematically studied by applying a RMP field, massive gas injection (MGI) and shattered pellet injection on J-TEXT. When the RMP-induced 2/1 LM is larger than a critical width, the MGI shutdown process can be significantly influenced. If the phase difference between the *O*-point of LM and the MGI valve is $+90^\circ$ (or -90°), the penetration depth and the assimilation of impurities can be enhanced (or suppressed) during the pre-thermal quench (TQ) phase and result in a faster (or slower) TQ. A secondary MGI can also suppress the runaway electron (RE) generation, if the additional high-Z impurity gas arrives at the plasma edge before TQ. When the secondary MGI has been applied after the formation of the RE current plateau, the RE current can be dissipated, and the dissipation rate increases with the injected impurity quantity but saturates with a maximum of 28 MA s^{-1}. The non-local transport is experimentally observed in the ion transport channel. The electron thermal diffusivity significantly increases with the ECRH power. Theoretical work shows that significant intrinsic current can be driven by electromagnetic turbulence, and the robust formation mechanism of the $E \times B$ staircase is identified from the Hasegawa–Wakatani system.

Keywords: J-TEXT tokamak, ECRH, resonant magnetic perturbation, disruption control, divertor, turbulence

(Some figures may appear in colour only in the online journal)

1. Introduction and technical improvements

As a long-term research program, the J-TEXT [1–3] experiments aim to develop fundamental physics and control mechanisms of high temperature tokamak plasma confinement and stability in support of successful operation of the ITER and the design of the future Chinese fusion reactor, CFETR. Recent research has highlighted the significance of the role that non-axisymmetric magnetic perturbations (MPs), so-called 3D MP fields, play in a fundamentally 2D concept, i.e. a tokamak. In this paper, the J-TEXT results achieved over the last two years, especially on the impact of 3D MP fields on magnetic topology, plasma disruptions and MHD instabilities, will be presented.

The following sub-sections in section 1 describe the successful operation of the electron cyclotron resonance heating (ECRH) systems and the poloidal divertor configuration, together with the upgrades of diagnostics. Section 2 summarizes the recent progress on MHD research, including the locked mode (LM) threshold, its control via a biased electrode, and three kinds of standing wave (SW) structures observed together with the magnetic island. Section 3 shows the progress on disruption control via various tools, concentrating on the suppression and dissipation of the runaway current. Section 4 describes the experimental and theoretical studies on the turbulence and transport. Finally, section 5 gives a summary and outlook.

1.1. Successful operation of ECRH systems

In order to increase the core electron temperature and study the non-inductive current drive on J-TEXT, the development of a 105 GHz/500 kW/1 s ECRH system has been initiated since 2017. The key microwave component in the ECRH system is a GYCOM gyrotron. Considering the toroidal field of J-TEXT, this system is designed to work at the X2 mode for plasma heating and non-inductive current drive. Figure 1 shows the layout of the ECRH system on the J-TEXT tokamak.

Based on the requirements for practical application, the detailed design for some of components in the ECRH system are accomplished. The launcher is expected to inject the microwave power generated by the gyrotron to the desired position in the plasma; the quasi-optical design and rotating mechanism design are of great significance. The launcher can be rotated in the toroidal and poloidal directions independently and the scanning range is no less than 20° [4], as shown in

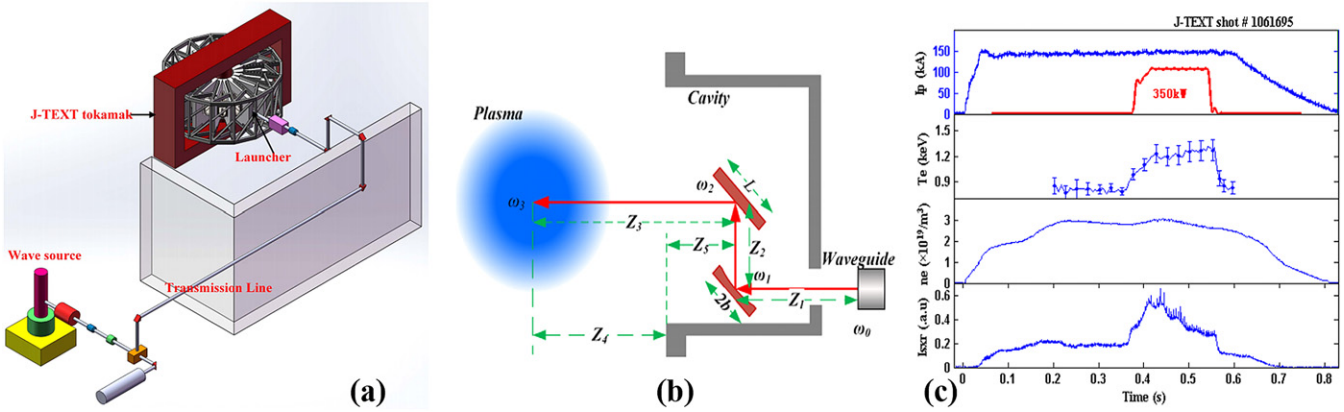

Figure 1. (*a*) Layout of the 105 GHz ECRH system on J-TEXT. (*b*) Schematic of the ECRH launcher. The microwave is reflected by the focusing mirror and the steering mirror in turn. (*c*) A typical discharge with 350 kW ECRH [4].

figure 1(*b*). To match the electron cyclotron wave (ECW) with the plasma efficiently, two polarizers—a linear polarizer and an elliptical polarizer—have been designed. The linear polarizer is mainly used to change the rotation angle of the wave, while the ellipticity of the wave is regulated by the elliptical polarizer [5]. Besides, to ensure the safe operation of the system, two types of fast protection units have been designed. One unit is for overvoltage and overcurrent protection, and another is for arc protection [6]. The ECRH system was successfully commissioned at the beginning of 2019. Figure 1(*c*) shows an example with 350 kW ECRH injected during the first commission phase. Currently, the ECW with a power of more than 400 kW has been successfully injected into the plasma, increasing the core electron temperature from 0.9 keV up to around 1.5 keV.

1.2. Operation of the poloidal divertor configuration

J-TEXT is equipped with a versatile set of poloidal divertor coils from TEXT-U [7], allowing for impurity exhaust and confinement studies over several different divertor configurations. These divertor coils, locating in the high-field side (HFS), can form four baseline divertor configurations with *X*-point(s) in the HFS, i.e. mid-plane single-null (MSN), double-null, upper single-null and lower single-null. The operation of J-TEXT with the divertor configuration was put forward in 2016. Along with the establishment of power supplies for divertor coils [8], the construction of relevant diagnostics [9, 10] and installation of the divertor target in the HFS, the plasma operation in the divertor configuration was first tested at the end of 2018.

The MSN divertor configuration has been realized for the first time in J-TEXT [11], as shown in figure 2. After the plasma current I_p reaches its flattop, the horizontal position of plasma, dx, is pushed outward for about 2 cm with respect to the routine center in the limiter configuration (figure 2(*b*)). Moving plasma toward the low-field side allows better stability during the transition to MSN, according to the in–out instability analysis [11]. Once dx reaches 2 cm at 0.25 s (figure 2(*e*1)), the divertor coil current I_{DV} starts to rise for 0.2 s and reaches its flattop for a duration of 0.1 s (figure 2(*c*)). With the ramping of I_{DV}, clear plasma shaping in the HFS mid-plane is visible (figure 2(*e*2)), and then the *X*-point is pushed into the vacuum vessel forming the divertor configuration at 0.446 s, as indicated by the sharp increase of floating potential measured in the HFS mid-plane (figure 2(*d*)) and the reconstructed flux surface in figure 2(*e*3). A successful MSN divertor configuration (figure 2(*e*4)) is maintained for 0.1 s. Figure 3(*a*) displays a typical image of the MSN operation. The 400 kW ECW has also been successfully injected into the diverted plasma. A clear increase of the core electron temperature is observed, and the increased heat flux toward the scrape-off layer (SOL) and the upper/lower strike points leads to intensive recycling and substantial release of impurity, as observed from the increase in visible light emission shown in figure 3(*b*).

1.3. Upgrade of diagnostics

Several diagnostics have been developed and upgraded on J-TEXT. A new 256-channel electron cyclotron emission imaging (ECEI) system was installed on J-TEXT at the end of 2019 [12]. It is an innovative design which first adopts many digital control components to realize intelligent remote control [13, 14]. The J-TEXT ECEI system consists of two receiving antenna arrays for different depth measurements at the same toroidal position, while operating in W-band (75–110 GHz) and F-band (90–140 GHz). Each antenna array has 16 independent vertical receivers covering eight radial detection volumes at different poloidal viewing. A multi-channel Doppler reflectometer (DR) system has been developed on J-TEXT. It has two sets of a four-channel, fixed frequency unit and a four-channel, tunable frequency unit which cover the 40–60 GHz frequency range. The DR system can provide information for plasma turbulence research, such as the density fluctuation, poloidal rotation, radial electric field and so on [15]. The vacuum ultraviolet (VUV) spectroscopy system on J-TEXT has also been upgraded to improve the temporal resolution for transport study. A micro-channel plate has been added to transmit the VUV light (30–200 nm) to visible light for acquisition by the electron multiplying charge-coupled device. Its temporal resolution is improved from 40 ms to about 2 ms [16]. These diagnostics will support future research on the

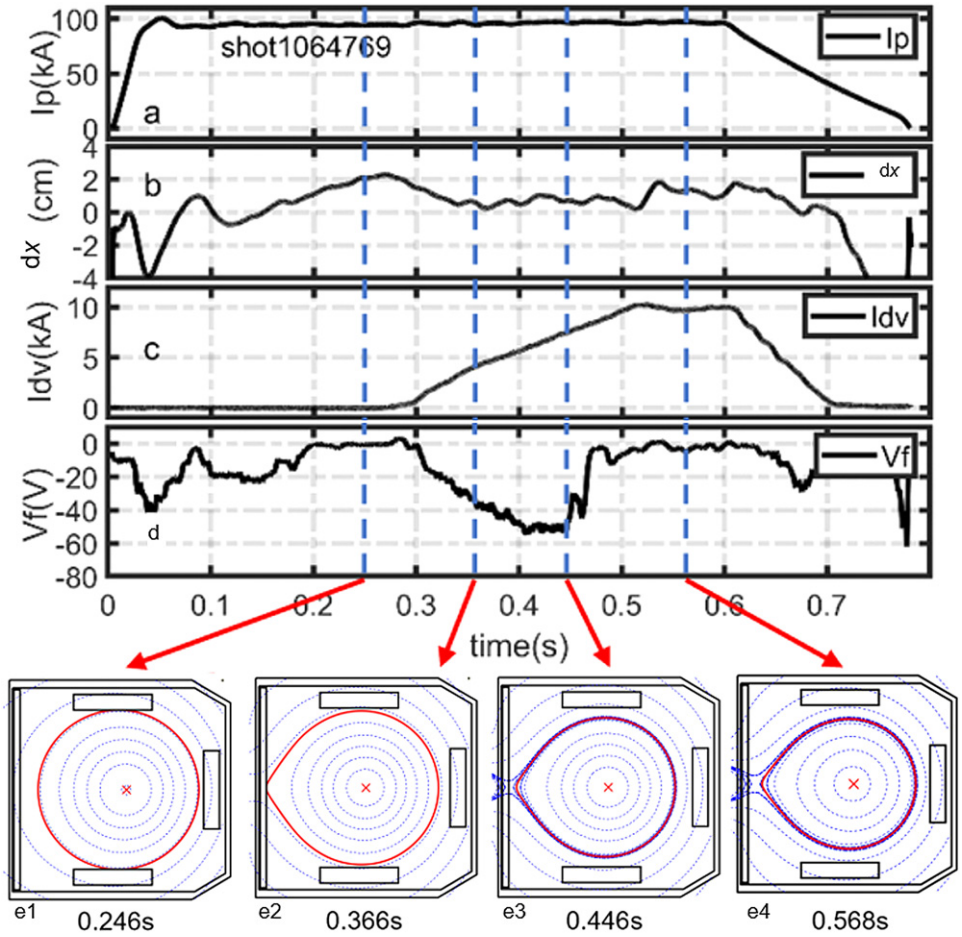

Figure 2. Typical waveforms of divertor configuration discharge on J-TEXT, with $I_p = 100$ kA, $B_T = 2$ T, $n_e = 1.5 \times 10^{19}$ m^{-3} [11]. The time evolution of (*a*) plasma current, (*b*) plasma horizontal displacement, (*c*) divertor coil current, and (*d*) floating potential measured on the mid-plane divertor target. (*e*1–4) The reconstructed flux surface contours at four time slices.

disruption physics, the turbulence, and in particular the interplay between the global MHD modes and the turbulence.

2. Progress in MHD research

The LM, especially the 2/1 LM, is one of the biggest threats to the plasma operation, since it can lead to major disruption. It is hence of great importance to estimate the threshold of its formation and to control it with high reliability. The LM is formed due to either the locking of a rotating tearing mode (TM) to the resonant component of the error field or the penetration of external resonant magnetic perturbations (RMPs). The latter is of great concern to the low density start-up phase of ITER. A non-monotonic density dependence is observed for the 2/1 LM threshold [17] on J-TEXT. Following the previous achievement of LM unlocking by rotating RMP [18], the electrode biasing (EB) has been applied successfully to unlock the LM from either a rotating or static RMP field [19]. In the presence of 2/1 LM, three kinds of SW structures [20–22] have been observed to share a similar connection to the island structure, i.e. the nodes of the SWs locate around the *O*- or *X*-points of the 2/1 island.

2.1. Density scaling of the RMP penetration threshold

It is previously found in J-TEXT that the 2/1 RMP penetration threshold, $b_{r,th}{}^{2/1}$, increases approximately with $n_e{}^{0.5}$ in the density range (0.7–2.7) $\times$ 10^{19} m^{-3} [23]. The density scaling exponent, α_n being around 0.5, is lower than the observations of $\alpha_n \sim 1$ in several other devices [24], however, $\alpha_n \sim 0.5$ is also observed in EAST [25]. With the installation of 12 new in-vessel RMP coils (two-turns) in 2017 [1], larger RMP amplitudes can be provided in J-TEXT. The density dependence of $b_{r,th}{}^{2/1}$ is then extended toward higher density (blue dots, figure 4(*a*)). It is found that once n_e is larger than a critical value, the penetration threshold dramatically decreases with further increase of n_e [17]. It is noted that the non-monotonic density dependence of $b_{r,th}{}^{2/1}$ is also observed in KSTAR and DIII-D [26]. The DIII-D case might be explained by the similar non-monotonic dependence of local density at $q = 2(n_e{}^{q2})$ on the core line-averaged density $\overline{n}_e$, while $n_e{}^{q2} \propto \overline{n}_e{}^{0.68}$ on J-TEXT.

The toroidal rotation at the $q = 2$ resonant surface, which plays an important role in the 2/1 RMP penetration yet being not included in the empirical scaling, also shows a similar non-monotonic density dependence (red diamonds, figure 4(*a*) in

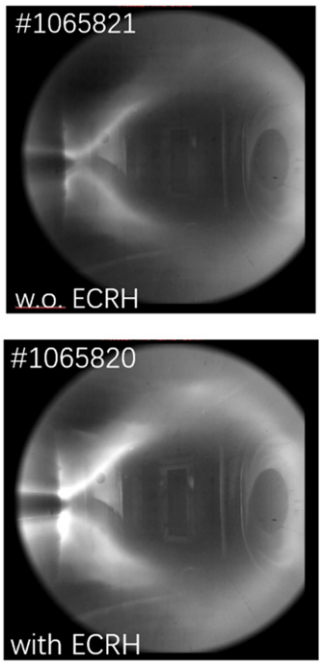

Figure 3. The visible emission photos for two MSN discharges with and without (w.o.) ECRH [11].

J-TEXT as that of $b_{r,th}{}^{2/1}$. The multiple linear regression provides a scaling in the form of $b_{r,th}{}^{2/1} \propto n_e{}^{-0.18\pm0.04} f_0{}^{1.04\pm0.25}$, where f_0 (the initial MHD frequency) is experimentally estimated by $f_0 = 0.3V_\Phi + 8.5$ [27]. This scaling reveals that there is only a weak or even no dependence of the 2/1 RMP penetration threshold on the density and a linear dependence on the plasma rotation. This result is not only important for the prediction of error field tolerance in fusion devices, but also opens a question on the role of density in the forced magnetic reconnection process in magnetized plasmas.

It would be interesting to study whether the density dependence of $b_{r,th}{}^{2/1}$ remains at other rational surfaces. The previous scaling for the 3/1 RMP penetration in the low-density range of (0.6–1.5) $\times$ 10^{19} m^{-3} [28] is extended to 4.5 $\times$ 10^{19} m^{-3} by using the two-turns RMP coils (figure 4(*b*)). It is found that $b_{r,th}{}^{3/1}$ also shows a similar non-monotonic dependence on density [29], and the roll-over density is at around 3 $\times$ 10^{19} m^{-3}. The variation of plasma rotation at the $q = 3$ surface will be compared in detail in the future. The penetration of 2/2 RMP [30] requires all the 24 RMP coils and their currents to approach the maximum available value. So the 2/2 RMP penetration is currently observed only at fairly low q_a (2.5–2.8) and low density ($<2 \times 10^{19}$ m^{-3}), which is lower than the roll-over density of the 2/1 RMP penetration [17]. Figure 4(*c*) shows a linear dependence of $b_{r,th}{}^{2/2}$ on density. It is not yet clear how $b_{r,th}{}^{2/2}$ would change at higher density, since the density dependence of V_ϕ might be difference in the core ($q = 1$) and the edge ($q = 2$ or 3) plasma.

2.2. LM control via EB

The external momentum input has been applied to unlock the LMs either by rotating RMP [18] or by neutral beam injection (NBI) [31]. The EB is also an efficient method to modify the plasma rotation, and it is found to be capable of increasing or decreasing the TM frequency with positive or negative biasing on J-TEXT [32]. Recently, EB was applied to study its impact on LMs, and it successfully unlocked the LM [19] from either a static or rotating RMP field as summarized in figure 5. The static 2/1 RMP field is applied to lock the TM and to maintain its locking status for 200 ms (#1061441, blue lines). As the first demonstration of unlocking, the RMP amplitude is reduced to a smaller amplitude after locking, so that LM will not lead to major disruption. When the EB is applied at 0.39 s in #1061442 (red), the phase difference (figure 5(*b*)) between the LM and the 2/1 RMP increases in the ctr-I_p direction and the LM amplitude (figure 5(*c*)) decreases. The LM is unlocked when the phase difference reaches about $-95°$. The mode frequency then quickly increases from 0 to about 3 kHz, followed by a slow increase to about 4.5 kHz. Statistical analysis shows that the LM is easier to unlock with stronger EB current or weaker LM amplitude.

Remarkably, the synergy effect of the EB and the static RMP field can suppress the unlocked mode completely. With larger EB current in #1061447, the LM is unlocked earlier and it decays away after the unlocking. The mode frequency before its suppression is around 6 kHz, which is smaller than 7 kHz in the TM suppression cases with only EB [32]. If the negative EB is applied before the TM being locked to external static RMP, it can stop the mode locking process by abruptly increasing the TM frequency and lead to the suppression of TMs (#1045120). The external momentum input from negative EB might counteract the braking effect of RMP, and hence the suppression effect of static RMP on TM is possible at lower TM frequency, compared to that reported previously for RMP alone [33].

2.3. SWs in the presence of magnetic islands

SWs have been widely observed in tokamak plasmas. In the J-TEXT experiments, three kinds of SW structures have been observed in the presence of large 2/1 magnetic islands, which can be either rotating at a few kHz or locked to the error field/RMP.

The first SW is identified to be the forced oscillation of the island phase [20] due to the application of an RMP field rotating at a few kHz (e.g. 1–6 kHz). Figures 6(*a*) and (*b*) display an example where a 6 kHz rotating RMP is applied to a plasma with slowly rotating 2/1 TM. The rotating RMP induces an EM torque on the TM and leads to the phase oscillation of TM, $\delta\xi_{TM}$. The plasma responses to rotating RMP is equal to the product of $\delta\xi_{TM}$ and the poloidal gradient of the plasma parameters, e.g. $\partial b_\theta{}^{2/1}/\partial\theta$ or $\partial T_e/\partial\theta$. Since $b_\theta{}^{2/1}$ has a maximum or minimal at the *O*- or *X*-point, the magnetic response δb_θ is around 0 at the *O*-/*X*-points, and changes sign on the two sides of *O*-/*X*-points. This then forms the observed SW structure, which has nodes around the *O*-/*X*-points, as shown in figure 6(*a*). The T_e response at 6 kHz were zero or minimal when $\partial T_e/\partial\theta \sim 0$, i.e. inside the magnetic island, or outside the magnetic island but at the same poloidal positions as the *O*-/*X*-points.

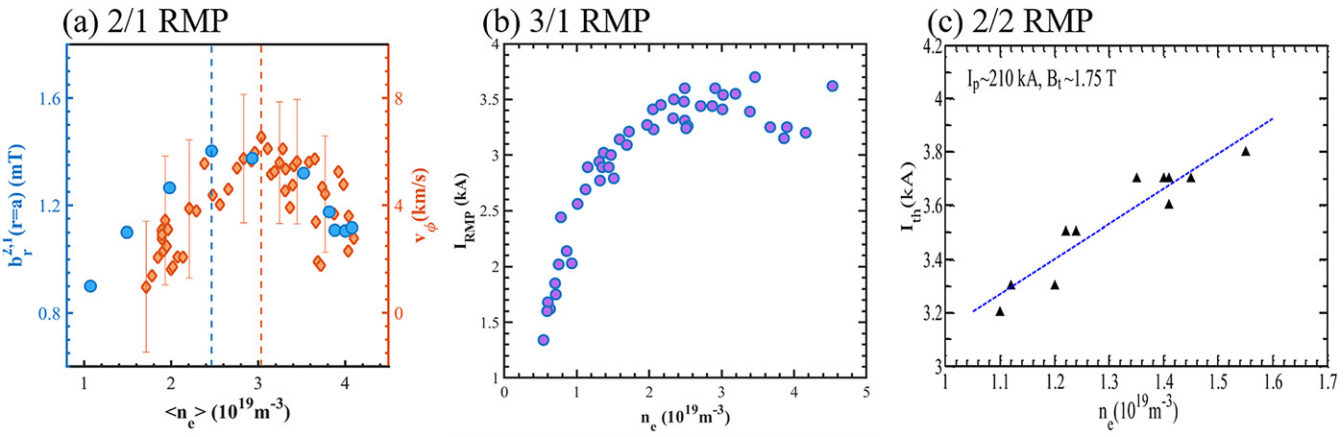

Figure 4. Density scaling of the penetration threshold of RMP, with dominant resonant component at m/n = (*a*) 2/1 [17], (*b*) 3/1 and (*c*) 2/2 [30].

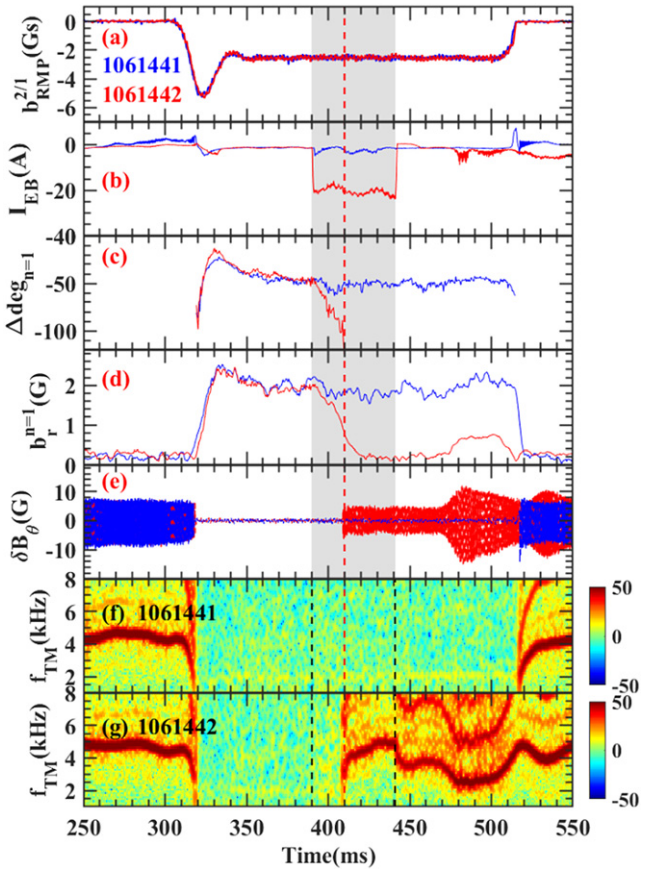

Figure 5. Unlocking of LM by EB [19]. Time evolutions of (*a*) the 2/1 component RMP amplitude, (*b*) EB current, (*c*) the phase difference between $n = 1$ LM and 2/1 RMP, (*d*) LM amplitude, (*e*) high frequency component (>0.5 kHz) of the poloidal MP (δB_θ), (*f*) and (*g*) the frequency spectrum from Mirnov probes showing the 2/1 mode frequency for shots 1061441 and 1061442. The shaded region shows the time period of applied EB. The red dashed line shows the time of mode unlocking for shot 1061442.

The second kind of SWs are the so-called beta-induced Alfvén eigenmodes (BAEs) [21] at 20–50 kHz observed with a locked or rotating magnetic island. BAEs have been widely observed with counter-propagating waves, and form a SW structure in the island rest frame [34, 35]. It is found in J-TEXT that the nodes of BAEs also locate at the *O*-/*X*-points of the magnetic island, as shown in figures 6(*c*) and (*d*). This feature is also found later in EAST [36].

The SW structure of BAEs has been explained by some theoretical studies [37, 38], however, solid experimental evidence to confirm the theoretical mechanism is still missing. It is noted that the spontaneously emerging BAEs and the artificial SWs induced by rotating RMP share a similar connection to the island structure, i.e. the nodes of the SWs locate around the *O*- or *X*-points of the 2/1 magnetic island. This connection might be a key to understand the BAEs. Moreover, a third SW [22] has been observed to appear spontaneously at ~3 kHz without any external 3 kHz RMP field. It also has nodes around the *O*-/*X*-points, and preliminary analysis indicates that it might be due to the spontaneous oscillation of island phase at 3 kHz. Future comparison between the second SW, i.e. BAEs, and the third SW would be important to reveal the mechanism of their formation.

3. Progress on disruption control

Disruption may cause excess heat loads, significant halo currents, and runaway electrons (REs), etc, which can damage the first wall and the machine, hence possibly leading to extensive down-time. So, disruption is considered to be one of the most urgent problems to address for future tokamaks. The control and mitigation of disruption is essential to the safe operation of ITER and future fusion reactors. In this section, we summarize the recent J-TEXT studies on the control of disruption triggered by massive gas injection (MGI), focusing on the RE current suppression and dissipation. RE suppression has been achieved by a secondary MGI [39], the magnetic island seeded via the RMP penetration [40–43] or magnetic energy transfer (MET) [44, 45], while the dissipation of the RE plateau is achieved by a secondary MGI [46, 47], a minus loop voltage [48] or a shattered pellet injection (SPI) [49].

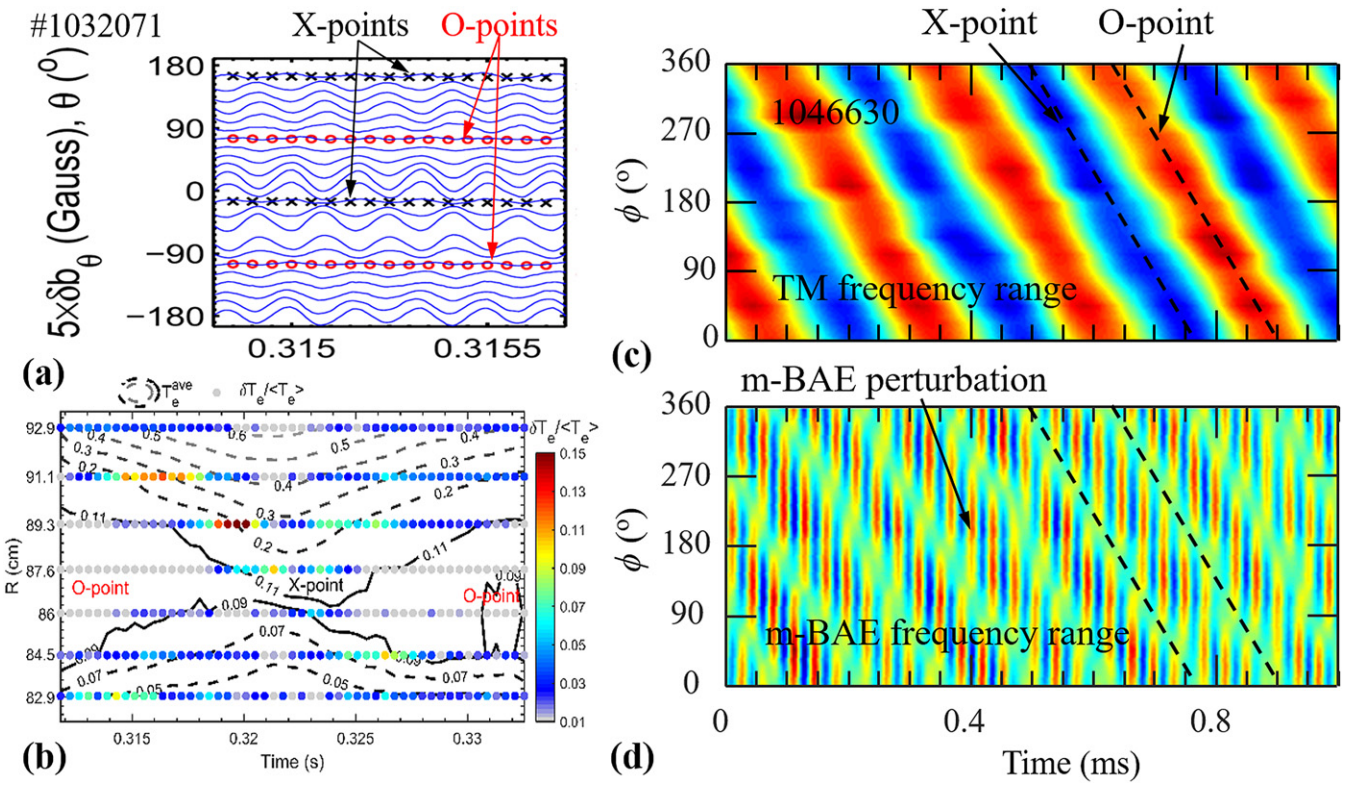

Figure 6. The time evolutions of two types of SW structures observed in J-TEXT. (1) The external 6 kHz rotating RMP induces a SW response [20] in both magnetic signals (*a*) and electron temperatures (*b*) in discharge #1032071. (2) The BAEs [21] show an SW structure with the nodes (*d*) locating at the *O*- and *X*-points (*c*) of the 2/1 magnetic island.

3.1. Suppression of runaway current by MGI and MET

MGI has been widely applied and proven to be a feasible way to mitigate the disruption. For future large-scale devices, a large quantity of the injected impurity may be needed. However, the injection efficiency of the massive impurity injection is limited by the injection rate and the assimilation efficiency, and hence RE generation might not be totally suppressed with an insufficient single injection of impurities. Runaway electrons on J-TEXT have converted a large fraction of the pre-disruption plasma current following an MGI-induced disruption, as shown by the black line in figure 7(*a*). In order to suppress the formation of the runaway current, a secondary gas injection from an additional valve (MGI2) with a delay time to the valve of the disruption mitigation system (MGI1) has been performed on J-TEXT [39], as summarized in figure 7. If the time when the additional high-Z impurity gas arrives at the plasma edge, $t_{\mathrm{arrival,MGI2}}$, is before the thermal quench (TQ), the runaway current (I_{RE}) can be significantly suppressed (magenta line) by weakening the primary RE generation, leading to a 90% reduction with respect to the reference RE current (I_{RE0}) without MGI2. If $t_{\mathrm{arrival,MGI2}}$ is during the current quench (CQ), I_{RE} can be partially suppressed (cyan line) by weakening the avalanche RE generation, leading to a 40%–80% reduction with respect to I_{RE0}.

An alternative path to suppress the RE generation would be to reduce the toroidal electric field, which is induced by the fast CQ. Significant reduction of $E_{||}$, or V_{loop}, and the suppression of RE have been achieved on J-TEXT by MET [44], as shown in figure 8. The MET system (figure 8(*a*)) consists of the energy transfer coils (ETCs), which are strongly magnetically coupled with the plasma current, the energy absorbing unit (EAU) with a low resistance (10.3 mΩ), and a controlled switch, which connects the ETCs and EAU during the CQ. During the rapid plasma shutdown by MGI, a co-I_{p} current will be induced in the ETCs and transfer the magnetic energy to the EAU, which is outside the vessel. The MET system accelerates the CQ rate and reduces the toroidal electric field at the same time. With the increase of ETC current, the conversion fraction of runaway current is significantly reduced and the RE generation is completely suppressed when I_{ETCs} is above 6.5 kA (figure 8(*c*)). The MET provides a new idea to transfer the magnetic energy and to suppress runaway current for disruption mitigation in future devices.

3.2. Dissipation of runaway current

In the case where RE suppression is not successful, a large fraction of runaway current might form and hence is a great threat to the device. Developing a reliable second defense method to dissipate RE current is also necessary. Several methods have been studied on J-TEXT in order to dissipate the runaway current.

The RE current plateau is formed by the first Ar MGI, and then the secondary Ar/Kr MGI has been applied to dissipate the RE current on J-TEXT [46]. The dissipation efficiency, characterized by the decay rate of RE current ($\mathrm{d}I_{\mathrm{RE}}/\mathrm{d}t$), is found to increase with the increase of injected impurity

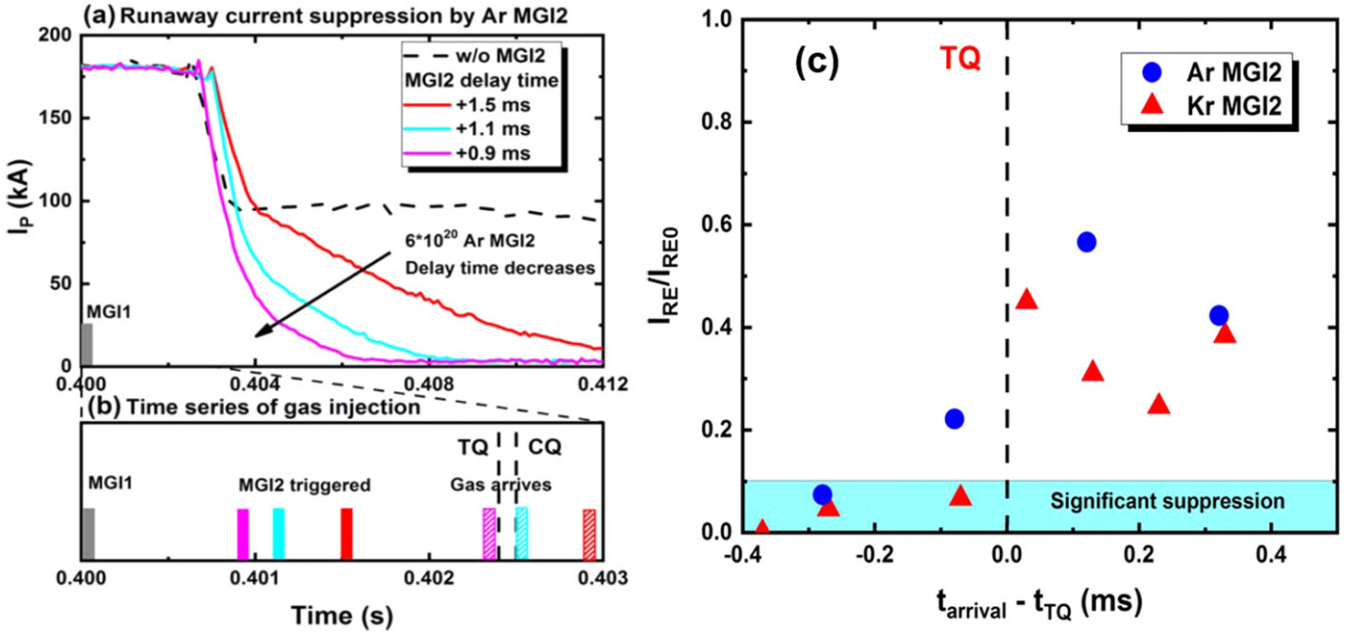

Figure 7. Runaway current suppression by a secondary MGI (MGI2) injected with different delay time after the first MGI, which triggers the disruption. (*a*) Time evolution of I_p decay caused by argon MGI2, (*b*) the time sequence of MGI1 trigger, MGI2 trigger, MGI2 arriving at plasma edge, TQ and CQ corresponding to (*a*). (*c*) The runaway currents with MGI2 versus the relative MGI2 arrival times of the argon and krypton cases. The reference RE current (I_{RE0}) is indicated by the black dashed line in (*a*) to be 100 kA [39].

quantity, N_{inj}, as shown in figure 9. However, the dissipation efficiency saturates with a maximum of $dI_{RE}/dt \approx 28$ MA s^{-1}, when N_{inj} exceeds 2×10^{21}. This saturation is shown to be mainly due to the decrease of the impurity assimilation rate when N_{inj} exceeds 2×10^{21}. A simplified estimation shows that the increase of l_i during the dissipation phase can lead to further slowing down of the runaway current dissipation. The effect of SPI on runaway current dissipation in J-TEXT has also been studied and compared with a similar amount of Ar MGI injection. With an argon quantity of about 2.12×10^{21}, SPI dissipates the RE current at a rate of about 12 MA s^{-1}, slower than that with MGI (18 MA s^{-1}) [49]. The slower RE dissipation of SPI might be due to the smaller injection speed of the shattered pellets (150–300 m s^{-1}); analysis and experiments will be continued to understand this effect. The results may have important implications for ITER disruption mitigation.

As another possible auxiliary method to dissipate the RE current, controlling the $E_{||}$ via an ohmic (OH) field, has been performed to study the soft landing of RE current on J-TEXT [48]. Figure 10 displays a typical comparison of three discharges with different loop voltage. It is found that the RE current decreases faster with lower loop voltage. With optimized horizontal displacement control of the RE beam, the toroidal electric field has been scanned from 1.6 to -0.3 V m^{-1} during the RE plateau phase. The dissipation rate by the OH field can reach a maximum value of 3 MA s^{-1}.

3.3. Impact of RMP on MGI-triggered disruption

During the MGI shutdown process, the external applied RMP field might play various roles, either enhancing [50] or suppressing [51] the RE production, depending on the RMP amplitude. Recent studies on J-TEXT reveal more features of the impact of RMP on MGI-triggered disruptions.

Without RMP, RE generation can be suppressed once n_e is larger than a critical threshold. This n_e threshold is found to be reduced by applying a moderate RMP field, as shown in figure 11 [40]. It is noted that in this case the RMP does not penetrate and hence no large locked island exists before the MGI. If the RMP is too strong or n_e is too low, the RE might also be suppressed due to the impact of locked island [51].

Both the phase and width of the RMP-induced 2/1 locked island are found to influence the MGI shutdown dynamics and RE generation. When the RMP-induced 2/1 LM is larger than a critical width, the MGI shutdown process can be significantly influenced. If the phase difference between the *O*-point of LM and the MGI valve is $+90°$ (or $-90°$), the penetration depth and the assimilation of impurities can be enhanced (or suppressed) during the pre-TQ phase and result in a faster (or slower) TQ [41]. Besides, the toroidal radiation asymmetry is observed to be worse in the case with LMs compared to the case without RMP.

Numerical studies on the role of RMP during MGI shutdown process are also performed with the 3D MHD code NIMROD [52]. In the modeling, the locked islands are preseeded by the RMP penetration before MGI. Both the phase [42] and amplitude [43] of these locked islands are varied in the simulations.

By varying the locked island phases, the RE confinement is found to be drastically affected during the TQ phase, as shown in figure 12. The ratio of remaining RE can be described by an $n = 1$ dependence on the toroidal phase of the locked island (figure 12(*b*)) [42]. The optimized phase difference for runaway suppression is predicted to be $\phi_{MGI} - \phi_{n=1} = 90°$.

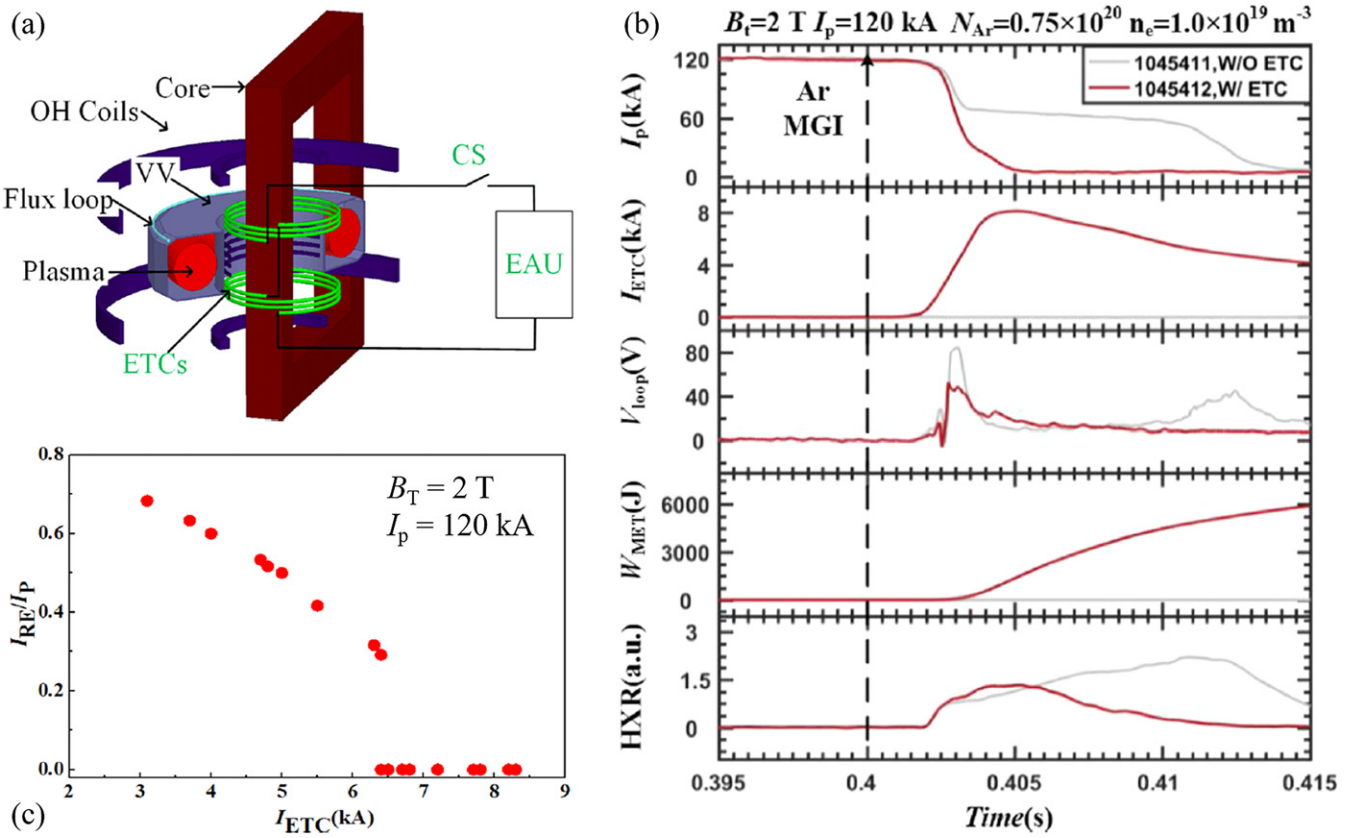

Figure 8. (*a*) Schematic of the MET system in J-TEXT. (*b*) Typical experimental result of runaway suppression by MET with $I_{ETC} = 8$ kA. (*c*) The influence of I_{ETC} on RE current fraction and suppression threshold [44].

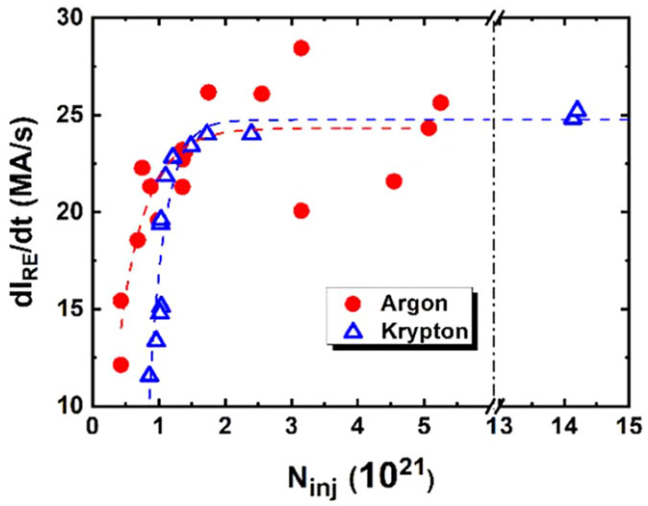

Figure 9. The runaway current dissipation rate versus the injected impurity quantity N_{inj} [46].

Further comparisons reveal the discrepancy in the evolution of the flux surface at various $\phi_{MGI} - \phi_{n=1}$, which greatly depends on the evolution of MPs induced during the disruption. The RE confinement is also found to vary non-monotonically with the width of the pre-seeded 2/1 locked island, as shown in figure 13 [43]. With a small pre-existing island width ($w_0/a < 0.11$), the RE remaining ratio is reduced compared to the case without an island (red dot), indicating the mitigation of REs. When w_0/a is sufficiently large, the loss of REs can already be clearly observed before TQ, and further loss of REs till CQ can lead to a much smaller ratio of remaining REs. With $w_0/a > 0.31$, this ratio decreases toward 0, indicating the suppression of REs. For a medium island width ($0.11 < w_0/a < 0.25$), the RE remaining ratio is larger than the case without a pre-existing island. During the disruption processes, the growth of MHD modes leads to an increase of MPs $\delta B^{n=1}/B$, and once $\delta B^{n=1}/B$ exceeds 4–6 $\times$ 10^{-3} the fraction of confined REs starts to decrease [43]. The time duration of $\delta B^{n=1}/B$ exceeding 4–6 $\times$ 10^{-3} is found to be a key for RE loss, and this duration is smallest for the medium island width case.

Those results suggest that the 3D effect between the injected impurities and the 2/1 LM is important during the disruption mitigation process.

4. Turbulence and transport study

4.1. Observation of non-local effects in ion transport channel

Following the previous observation of non-local transport (NLT) in multiple transport channels (electron temperature, particle, and momentum) [53], recent J-TEXT experiments reveal that the ion transport channel shows a similar non-local response to the electron transport channel [54], owing to the

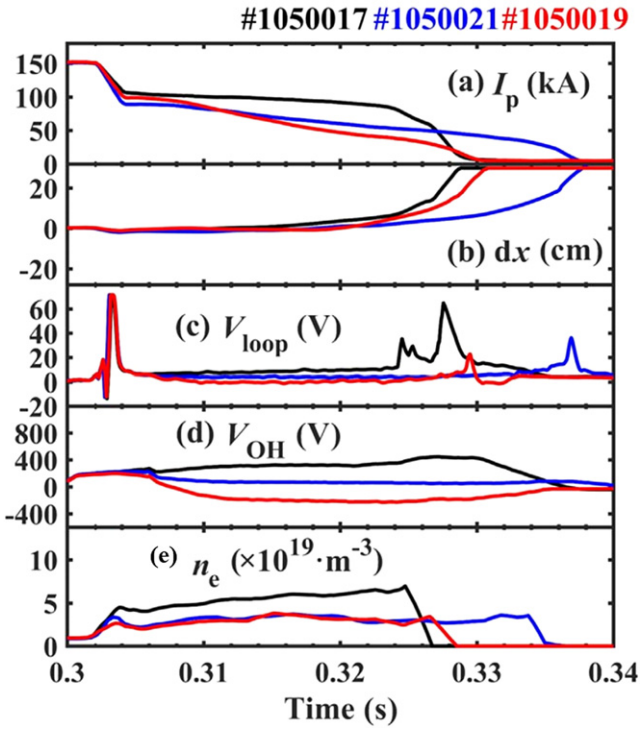

Figure 10. Evolution of RE currents in three discharges with different loop voltage [48].

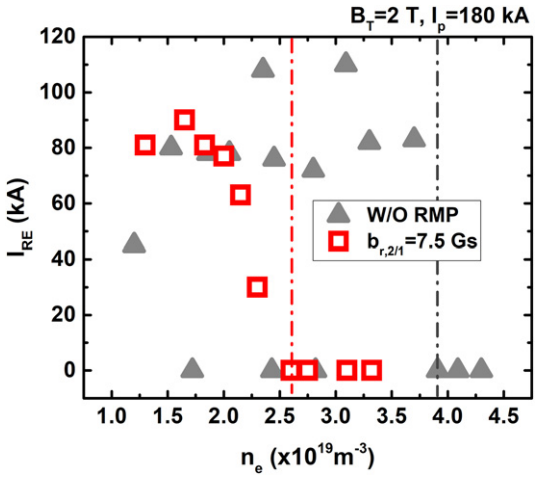

Figure 11. The amplitude of runaway current with different pre-disruption electron density for cases with 2/1 RMP (red squares) and without RMP (gray triangles) [40].

improved temporal resolution of the ion temperature measurement to millisecond level. Very fast ion temperature decreases are observed in the edge, while the ion temperature in the core promptly begin to rise after injection of the cold pulse. Moreover, the cut-off density is also found for the ion non-local effect. The experimentally observed density fluctuation in a high frequency ranging from 500 kHz to 2 MHz is obviously reduced in the whole plasma region during the NLT phase.

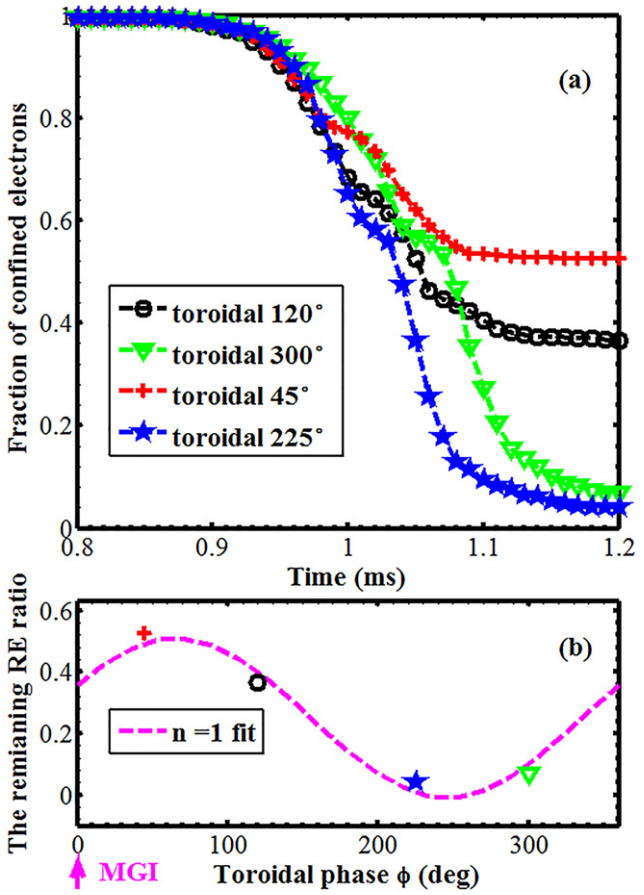

Figure 12. Effect of different phases of pre-seeded 2/1 locked islands on RE confinement obtained from the NIMROD simulation. (*a*) Fraction of confined REs versus time (ms) for four island phases. (*b*) The dependence of the remaining RE ratio after the TQ on the toroidal phase of 2/1 islands [42].

4.2. Electron thermal transport with ECRH

Electron thermal transport has been compared for ohmic plasma and ECRH L-mode plasma. It is found that the electron thermal diffusivity χ_e increases with the ECRH power at a constant rate of around 9 m^2s^{-1} per MW, as shown in figure 14. The bandwidth of medium scale temperature fluctuation also becomes broader as the ECRH power increases. The Gyrokinetic Electromagnetic Numerical Experiment (GENE) simulation [55] shows that the low and medium scale turbulence translate from trapped electron mode (TEM) and ion temperature gradient (ITG) mixed mode in ohmic plasma to pure TEM mode in ECRH plasma. In the ohmic plasma, χ_e is found to decrease with increasing plasma density, while with 400 kW ECRH χ_e is almost at the same level for different plasma density. It indicates the electron temperature gradient (ETG) mode may dominate the electron heat transport in the high density ECRH plasma [56].

4.3. Theoretical study on the turbulence

The intrinsic current driven by electromagnetic turbulence in the pedestal region has been analytically investigated [57]. It is found that the intrinsic current density driven by the residual

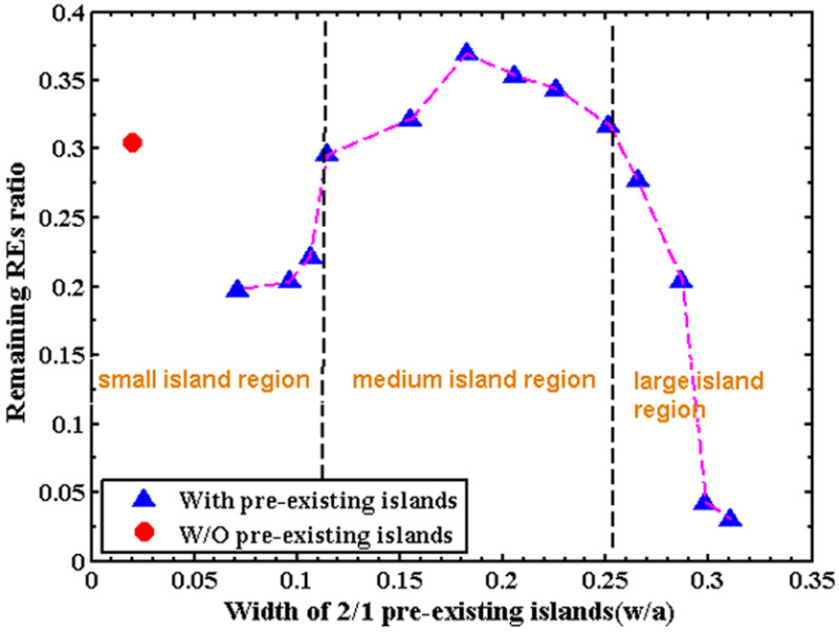

Figure 13. Dependence of the remaining RE ratio on the width of pre-seeded 2/1 locked islands obtained from the NIMROD simulation [43].

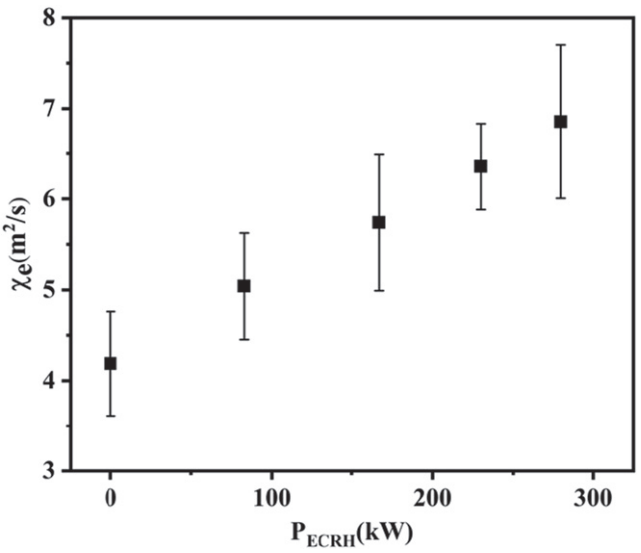

Figure 14. The electron thermal transport diffusivity (χ_e) versus different ECRH power [55].

turbulent source, which is analogous to the intrinsic rotation driven by electromagnetic (EM) turbulence [58, 59], is negligible as compared to that driven by the residual turbulent flux. Therefore, the modification of local current density could be significant. For the EM electron drift wave in the ITER pedestal region, the ratios of intrinsic current density driven by residual turbulent flux and by turbulent source to the bootstrap current density scales to $T_e^{3/4}T_i/n_e$ and T_eT_i/n_e, respectively [57].

We investigated the drift loss of fast ions induced by the combination of the RMP field and the strong radial electric field (E_r) in a tokamak pedestal [60]. The equations of the bounce/transit-averaged radial drift induced by the RMP field and the toroidal precession modified by the strong E_r have been derived. The strong E_r in the pedestal significantly reduces the toroidal precession frequency of deeply trapped fast ions, which plays a key role in the loss of trapped fast ions. This implies that the confinement of fast ions generated by perpendicular NBI might be worse than that by tangential NBI in the pedestal region. Furthermore, the drift loss time is smaller than the slowdown time by three orders of magnitude for DIII-D pedestal parameters, which points out a possible important mechanism for the loss of deeply trapped fast ions.

The parallel velocity shear (PVS)-driven Kelvin–Helmholtz instability [61, 62] can be developed in magnetic fusion plasmas with high PVS, and it is found that the excitation of PVS turbulence is one of the possible explanations for experimental observation of impurity accumulation in the present tokamaks with NBI heating, for both fully ionized, light impurities (such as Be^{4+}, C^{6+}, Ne^{10+} from the intrinsic plasma–wall interaction or external injection) and heavy tungsten (W), while increasing the electron density gradient is favorable for stabilizing PVS mode and reducing the accumulation of impurities, because the inward impurity flux driven by PVS turbulence is significantly reduced [63]. Beside, the role of PVS turbulence on the removal of helium ash is also investigated. When the density profile of helium ash is comparable or steeper than that of electrons, the normalized flux of helium ash is outward since the diffusivity is larger than the inward convective velocity.

A mean field model, which is derived from the Hasegawa–Wakatani equation [64], is used to study the scale selection and feedback loops for the formation and sustainment of a staircase structure pattern [65]. It is mainly found that the principle feedback loop is through the nonlinear dependence of mixing length on electron density gradient, rather than $\vec{E} \times \vec{B}$ shearing. When the zonal shear and mean shear are comparable,

there will exist a non-uniform staircase structure, and the minimal step scale is selected by competition between the initial density gradient (i.e. drive) and diffusive dissipation. Moreover, it is also found that finite turbulence spreading is necessary to form the staircase structure, while moderate enhancement of turbulence spreading will wash out this pattern. Then, it is concluded that the staircase-like structure in density (as well as in potential vorticity) is formed by self-sharpening of modulations, and the electron density gradient-dependent mixing feedback is a natural route to enhanced confinement regimes, thus it acts as a candidate trigger mechanism for the L–H transition.

5. Summary and outlook

Over the last two years, three major achievements have been made on J-TEXT in support of expanded operation regions and diagnostic capabilities. (1) The successful commission of the 105 GHz/500 kW/1 s ECRH system increasing the core electron temperature from 0.9 keV up to around 1.5 keV. (2) The poloidal divertor configuration with an *X*-point in the HFS has been achieved. In particular, the 400 kW ECW has also been successfully injected into the diverted plasma. (3) A 256-channel ECEI diagnostic system and two sets of four-channel DBS diagnostics have been successfully developed on J-TEXT, allowing detailed measurement of the electron temperature and density fluctuations for turbulence and MHD research.

The LM, especially the 2/1 LM, is one of the biggest threats to the plasma operation, since it can lead to major disruption. It is hence important to study its formation and control. Both the thresholds of 2/1 and 3/1 LM are observed to vary non-monotonically with electron density. The EB has been applied successfully to unlock the LM from either a rotating or static RMP field. Remarkably, the synergistic effect of the EB and RMP field can suppress the unlocked mode completely. In the presence of 2/1 LM, three kinds of SW structures have been observed to share a similar connection to the island structure, i.e. the nodes of the SWs locate around the *O*- or *X*-points of the 2/1 island. The SWs can either be actively induced by the external rotating RMP field at its frequency, or emerge spontaneously at 20–50 kHz (for BAEs) or $\sim$3 kHz. A systematic comparison among the three kinds of SWs might reveal the mechanism for the formation of these SWs.

The control and mitigation of disruption is essential to the safe operation of ITER, and it has been systematically studied by applying a RMP field, MET, MGI and SPI on J-TEXT. When the RMP- induced 2/1 LM is larger than a critical width, the MGI shutdown process can be significantly influenced. If the phase difference between the *O*-point of LM and the MGI valve is $+90^\circ$ (or -90°), the penetration depth and the assimilation of impurities can be enhanced (or suppressed) during the pre-TQ phase and result in a faster (or slower) TQ. During the MGI shutdown process, the RE generation can be suppressed once n_e is larger than a critical threshold. This n_e threshold can be reduced by applying an RMP field. The MGI shutdown process with a pre-seeded locked island is also studied numerically using NIMROD, and the dependence on the island phase and amplitude show good agreement with the above experimental observations. A secondary MGI following shortly after the first MGI can also suppress RE generation, if the additional high-Z impurity gas arrives at the plasma edge before TQ. By transferring the magnetic energy carried by the plasma current to the external coils during disruption, the toroidal electric field is significantly reduced and RE suppression can be achieved with sufficiently large ETC current. When the secondary MGI has been applied after the formation of the RE current plateau, the RE current can be dissipated, and the dissipation rate increases with the quantity of injected impurity; a maximum of 28 MA s^{-1} runaway dissipation rate has been achieved on J-TEXT. These results suggest that the 3D effect, the transfer and exhaust of magnetic energy, and the impurity injection strategy are important during the disruption mitigation process. They may have important implications for ITER disruption mitigation.

The NLT is experimentally observed in the ion transport channel. The electron thermal diffusivity significantly increases with the ECRH power. Experimental measurement and GENE simulation indicate that the ETG may dominate the electron heat transport in the high density ECRH plasma. Theoretical work shows that significant intrinsic current can be driven by electromagnetic turbulence, and the robust formation mechanism of $E \times B$ staircase is identified from the Hasegawa–Wakatani system.

In the next two years, these newly developed diagnostics and auxiliary systems, e.g. ECE-imaging, VUV spectrometer, and Doppler reflectometry, will be beneficial for studying the formation and control of LMs, the coupling of multi-MHD modes, the interplay between the magnetic island with turbulence measured with temperature and density fluctuations, the turbulence behavior approaching the density limit, etc. The plasma operation with ECRH or poloidal divertor configuration will become more mature and it will inspire further research on plasma heating, current drive, the control of magnetic island and sawtooth, fast electron-related physics (e.g. increasing the RE seeds), disruption prevention or mitigation, boundary physics, etc.

Acknowledgments

This work is supported by the National MCF Energy R & D Program of China (Contract Nos. 2018YFE0309100, 2018YFE0310300), the National Key R & D Program of China (No. 2017YFE0302000) and the National Natural Science Foundation of China (Nos. 11775089, 11905077, 11905078, 11905079, 11905080, 12075096, 12047526, 11675059, 11605066 and 51821005).

Appendix

The J-TEXT team

Yonghua Ding[1], Yunfeng Liang[1, 2, 3], Yuan Pan[1], Kenneth William Gentle[4], Xiwei Hu[1], Kexun Yu[1], Qingquan Yu[5], Donghui Xia[1], Ming Zhang[1], Li Gao[1], Lu Wang[1],

Zhongyong Chen[1], Zhijiang Wang[1], Zhonghe Jiang[1], Zhipeng Chen[1], Zhoujun Yang[1], Zhifeng Cheng[1], Xiaoqing Zhang[1], Minghai Liu[1], Tao Xu[1], Ping Zhu[1], Wei Jiang[6], Lin Yi[6], Ya Zhang[7], Bo Rao[1], Qiming Hu[8], Wei Zheng[1], Shaoxiang Ma[1], Yong Yang[1], Chuan Li[1], Nengchao Wang[1], Jianchao Li[9], Xiaolong Zhang[10], Mingxiang Huang[11], Weixin Guo[1], Wei Yan[1], Da Li[1], Jie Huang[1], Weijun Wang[1], Mei He[1], Qing Zhao[1], Jiayu Xu[1], Gangyi Zhou[1], Weigang Ba[1], Cheng Yang[1], Junjie Yao[1], Chuliang Wang[1], Bo He[1], Jingwei Fu[1], Meiling Liang[1], Yehong Guan[1], Hongyan Wu[1], Peng Shi[12], Zhifang Lin[13], Hai Liu[14], Ge Zhuang[15], Weixing Ding[15], Tao Lan[15], Youwen Sun[3], Long Zeng[3], Shaocheng Liu[3], Huaxiang Zhang[3], Liang Liao[3], Wulyu Zhong[16], Zhongbing Shi[16], Min Jiang[16], Yunbo Dong[16], Min Xu[16], Aike Wang[16], Linzi Liu[16], Ruihai Tong[16], Jun Cheng[16], Lin Nie[16], Rui Ke[16], Ting Long[16], Hui Li[16], Jianqiang Xu[16], Zengchen Yang[16], Jie Wen[16], Anshu Liang[16], Yipo Zhang[16], Yifan Wu[16], Chengyuan Chen[16], Kaijun Zhao[17], Yuejiang Shi[18], He Huang[4], Max Austin[4], Sanggon Lee[19], Neville C. Luhmann Jr[20], Calvin W. Domier[20], Yilun Zhu[20], David L. Brower[21], Jie Chen[21], K. Ida[22], Y. Suzuki[22], Y. Takemura[22], K. Nagasaki[23], P. Drews[2], A. Knieps[2], Xiang Han[2], A. Krämer-Flecken[2], M. Henkel[2], Lizhi Zhu[1], Xiaoming Pan[1], Yiren Zhu[1], Wen He[1], Yunong Wei[1], Mao Li[1], Xianli Xie[1], Xiutao Huang[1], Xueliang Zhang[1], Jiyang He[1], Zeng Zhong[1], Yinan Zhou[1], Zhuo Huang[1], Ruo Jia[1], Nianheng Cai[1], Chengxi Zhou[1], Ying He[1], Yue Peng[1], Qi Zhang[1], Hanhui Li[1], Pengyu Wang[1], Xin Xu[1], Song Zhou[1], Dongyu Wang[1], Jiawei Li[1], Cancan Rong[1], You Li[1], Feiyue Mao[1], Xiaoyi Zhang[1], Jie Yang[1], Conghui Lu[1], Junli Zhang[1], Yiwei Lu[1], Rumeng Wang[1], Hongqi Zhang[1], Yingqin Zeng[1], Chengshuo Shen[1], Jiangang Fang[1], Zhengkang Ren[1], Guodong Zhang[1], Xixuan Chen[1], Fangyuan Ma[1], Malik Sadam Hussain[1], Abba Alhaji Bala[1], Tingting Yang[1], Conghui Lu[1], Minghui Xia[1], Huaiyu Yang[1], Jing Huang[1], Lai Peng[1], Zebao Song[1], Ming Chen[1], Xueqing Zhao[1], Yikun Jin[1], Qinxue Cai[1], Hao Zhou[1], Xiao Ma[1], Jingjun Zhou[1], Weiwei Zhang[1], Huapu Deng[1], Jie Hu[1], Duoqin Wang[1], Wei Li[1], Zichao Xu[1], Wei Zhang[1], Xin Ye[1], Changhong Li[1], Yuxing Wang[1], Lan Zhou[1], Jiapeng Xiao[1], Yixiong Zhang[1], Yizhe Tian[1], Aoxiang Wang[1], Haotian Huang[1], Fengqi Chang[1], Jing Zhou[1], Jingjing Xuan[1], Zhi Liu[1], Chengjin Qian[1], Tong Wang[1], Yuan Huang[1], Huaiyu Yang[1], Haotian Liang[1], Zhou Yang[1], Mingcong Zhu[1], Haisen Mo[1], Liuxiu He[1], Zhou Yang[1], Zheng Zhou[1], Xiong Tao[1], Zhigang Hao[1], Qiong Li[1], Jinyu Xiong[1], Huakun Cai[1], Mingzhu Zhang[1], Yaping Zhang[1], Yangming Zhao[1], Qiancheng Zhao[1], Wei Bai[1], Yu Zhong[1], Shaodong Jiao[1], Dongliang Han[1], Shiyi Peng[1], Jiaolong Dong[1], Qinglong Yang[1], Fan Gu[1], Zhaosu Wang[1], Hao Wang[1], Shu Yang[1], Yang Zhao[1], Wang Lin[1], Fan Guoyao[1], Kehong Dong[1], Xiehang Ren[1], Feng Li[1], Ce Deng[1], Feng Han[1], Jing Liu[1], Qiqi Wu[1], Fei Xie[1], Yujie Zhong[1], Zinan Wei[1], Wanjun Qing[1], Chu Han[1], Hui Ye[1], Xiaobo Zhang[1], Yingzhou Jiang[1], Lingke Mou[1], Chengyu Yang[1], Shuhao Li[1], Jianjun Yuan[1], Jiankun Hua[1], Haojie Chen[1], Xiaobo Liu[1], Wentong Shang[1], Guan Shengyuan[1], Chouyao Tang[1], Sheng Li[1], Zhangsheng Huang[1], Qinlin Tao[1], Jiamao Gao[1], Wenting Weng[1], Shouqi Xiong[1], Yuan Gao[1], Zhichao Zhang[1], Li Dingchen[1], Boliang Zhu[1], Fuyou He[1], Xinkun Ai[1], Feiyang Wu[1], Xianqian Zha[1], Guo Tong[1], Xiaohan Xie[1], Chuanxu Zhao[1], Ruiyang Xu[1], Fengming Xue[1], Weikang Zhang[1], Zixiao Jiao[1], Chupin Fu[1], Guo Chengzhi[1], Sifen He[1], Yixing Jiang[1], Xianghao Kong[1], Cunkai Li[1], Feng Li[1], Zhen Li[1], Jiaxing Liu[1], Renzhe Liu[1], Yiming Ma[1], Zitong Qu[1], Ye Tian[1], Wenshan Wang[1], Yuhan Wang[1], Zutao Wang[1], Dengfeng Xu[1], Qinghu Yang[1], Wendi Yang[1], Shimin Yu[1], Bangyou Zhu[1], Guangding Zhu[1], Xiating Mou[1], Xianlong Liu[1]

[1]International Joint Research Laboratory of Magnetic Confinement Fusion and Plasma Physics, State Key Laboratory of Advanced Electromagnetic Engineering and Technology, School of Electrical and Electronic Engineering, Huazhong University of Science and Technology, Wuhan 430074, China, [2]Forschungszentrum Jülich GmbH, Institut für Energie- und Klimaforschung—Plasmaphysik, 52425 Jülich, Germany, [3]Institute of Plasma Physics, Chinese Academy of Sciences, Hefei 230031, China, [4]University of Texas at Austin, Austin, TX 78712, United States of America, [5]Max-Planck-Institut für Plasmaphysik, D-85748 Garching, Germany, [6]School of Physics, Huazhong University of Science and Technology, Wuhan 430074, China, [7]Department of Physics, Wuhan University of Technology, Wuhan 430070, China, [8]Princeton Plasma Physics Laboratory, PO Box 451, Princeton, NJ 08543, United States of America, [9]Hubei Key Laboratory of Optical Information and Pattern Recognition, Wuhan Institute of Technology, Wuhan, 430205, China, [10]Advanced Energy Research Center, Shenzhen University, Shenzhen 518060, China, [11]College of Computer Science, South-Central University for Nationalities, Wuhan 430074, China, [12]United Kingdom Atomic Energy Authority (CCFE), Culham Science Center, Abingdon, Oxon, OX14 3DB, United Kingdom of Great Britain and Northern Ireland, [13]Jiangsu Normal University, School of Electrical Engineering & Automation, Xuzhou 221116, China, [14]Southwest Jiaotong University, Chengdu, China, [15]University of Science and Technology of China, Hefei 230026, China, [16]Southwestern Institute of Physics, Chengdu 610041, China, [17]College of Nuclear Science and Engineer, East China University of Technology, PO Box 330013, Nanchang, China, [18]Hebei Key Laboratory of Compact Fusion, Langfang 065001, China, [19]National Fusion Research Institute, Daejeon 305-333, Korea, Republic of, [20]University of California, Davis, CA 95616, United States of America, [21]University of California Los Angeles, Los Angeles, CA 90095, United States of America, [22]National Institute for Fusion Science, 509-5292 Toki, Japan, [23]Institute of Advanced Energy, Kyoto University, Gokasho, Uji, Kyoto 611-0011, Japan

ORCID iDs

Nengchao Wang https://orcid.org/0000-0001-6797-2398
Zhongyong Chen https://orcid.org/0000-0002-8934-0364
Zhipeng Chen https://orcid.org/0000-0002-8330-0070

Zhoujun Yang https://orcid.org/0000-0002-9141-7869
Zhonghe Jiang https://orcid.org/0000-0002-4971-080X
Lu Wang https://orcid.org/0000-0002-5881-6139
Qiming Hu https://orcid.org/0000-0002-8877-4988
Zhuo Huang https://orcid.org/0000-0001-7527-6464
Yuejiang Shi https://orcid.org/0000-0002-9572-3310
Weixin Guo https://orcid.org/0000-0001-7677-799X
Peng Shi https://orcid.org/0000-0002-1853-0726
Zhifeng Cheng https://orcid.org/0000-0001-6019-399X
Ping Zhu https://orcid.org/0000-0002-5773-8861
Minghai Liu https://orcid.org/0000-0002-8065-4404
Yong Yang https://orcid.org/0000-0001-7304-7529
Chuan Li https://orcid.org/0000-0003-4761-5160
Ming Zhang https://orcid.org/0000-0002-9372-4926
Q. Yu https://orcid.org/0000-0003-2722-4445

References

[1] Liang Y. *et al* 2019 *Nucl. Fusion* **59** 112016
[2] Zhuang G. *et al* 2011 *Nucl. Fusion* **51** 094020
[3] Ding Y.H. *et al* 2018 *Plasma Sci. Technol.* **20** 125101
[4] Zhang J.L., Xia D.H., Liu C.H., Wang Z.J. and Pan Y. 2020 *IEEE Trans. Plasma Sci.* **48** 1560
[5] Tian Y.Z., Xia D.H., Liu C.H. and Wang Z.J. 2019 *Fusion Eng. Des.* **146** 269
[6] Wang Z., Fan G., Xia D., Chen X. and Weng W. 2021 *IEEE Trans. Plasma Sci.* **49** 258
[7] Edmonds P. *et al* 1989 *Fusion Technol.* **1** 342–6
[8] Xie X. *et al* 2014 *Nucl. Fusion Plasma Phys.* **34** 80
[9] Chen Z., Li F., Zhuang G., Jian X. and Zhu L. 2016 *Rev. Sci. Instrum.* **87** 11D408
[10] Xia M., Chen Z., Deng H., Yang J., Zhu L., Xie X., Zhou Y. and Wang Z. 2019 *Fusion Eng. Des.* **146** 578
[11] Chen Z.P. *et al* 2021 Realization of divertor configuration discharge in J-TEXT tokamak *28th IAEA Fusion Energy Conference (FEC 2020)* (10–15 May 2021) (https://conferences.iaea.org/event/214/contributions/17447/)
[12] Xie X.L., Zhou J., Zhu Y., Pan X.M., Zhou H., Yu G., Luhmann N.C., Zhuang G. and Yang Z.J. 2020 *Fusion Eng. Des.* **155** 111636
[13] Pan X.M. *et al* 2016 *Rev. Sci. Instrum.* **87** 11E106
[14] Yang Z.J. *et al* 2020 *Fusion Eng. Des.* **153** 111494
[15] Ren X.H., Yang Z.J., Shi Z.B., Yang Z.C., Zha X.Q., Gao Y. and Zhang Z.C. 2021 *Rev. Sci. Instrum.* **92** 033545
[16] Zhang X.Y. *et al* 2021 *Rev. Sci. Instrum.* **92** 073503
[17] Huang Z. *et al* 2020 *Nucl. Fusion* **60** 064003
[18] Li D. *et al* 2020 *Nucl. Fusion* **60** 056022
[19] Chen Z.P. *et al* 2021 *Nucl. Fusion* **61** 02600
[20] Wang N. *et al* 2019 *Nucl. Fusion* **59** 026010
[21] Liu L. *et al* 2019 *Nucl. Fusion* **59** 126022
[22] Wang N.C. *et al* 2021 Observation of a 3 kHz standing wave in the presence of the quasi-static magnetic island on J-TEXT (Sitges, Spain 21–25 June 2021) (https://www.epsplasma2020.eu/) *47th EPS Plasma Physics Conf.*
[23] Wang N. *et al* 2014 *Nucl. Fusion* **54** 064014
[24] Buttery R.J. *et al* 1999 *Nucl. Fusion* **39** 1827
[25] Wang H.-H. *et al* 2018 *Nucl. Fusion* **58** 056024
[26] Park J.K. and Logan N.C. 2019 MDC-19 updates for ITER error field correction criteria *34th Meeting of the ITPA Topical Group on MHD Disruption and Control* (Garching, Germany) (https://www.ipp.mpg.de/Joint-ITPA)
[27] Yan W. *et al* 2018 *Plasma Phys. Control. Fusion* **60** 035007
[28] Hu Q. *et al* 2016 *Nucl. Fusion* **56** 092009
[29] Wang N.C. *et al* 2021 Formation and control of the 3/1 locked island in the plasma boundary on J-TEXT *10th Int. Workshop on 'Stochasticity in Fusion Plasmas (SFP)'* (Wuhan, China) (https://sfp2021.aconf.org/index.html)
[30] Li J. *et al* 2020 *Nucl. Fusion* **60** 126002
[31] Liang Y., Koslowski H.R., Krämer-Flecken A., Zimmermann O., Löwenbrück K., Bertschinger G. and Wolf R.C. 2007 *Nucl. Fusion* **47** L21
[32] Liu H., Hu Q., Chen Z., Yu Q., Zhu L., Cheng Z., Zhuang G. and Chen Z. 2017 *Nucl. Fusion* **57** 016003
[33] Jin W. *et al* 2013 *Plasma Phys. Control. Fusion* **55** 035010
[34] Buratti P., Smeulders P., Zonca F., Annibaldi S.V., Benedetti M.D., Kroegler H., Regnoli G. and Tudisco O. (The FTU-Team) 2005 *Nucl. Fusion* **45** 1446
[35] Liu L., He J., Hu Q. and Zhuang G. 2015 *Plasma Phys. Control. Fusion* **57** 065007
[36] Xu M. *et al* 2021 *Nucl. Fusion* **61** 036034
[37] Marchenko V.S., Panwar A., Reznik S.N. and Ryu C.M. 2016 *Nucl. Fusion* **56** 106021
[38] Cai H., Gao B., Xu M., Liu A. and Kong D. 2021 *Nucl. Fusion* **61** 036029
[39] Wei Y.N., Yan W., Chen Z.Y., Tong R.H., Jiang Z.H. and Yang Z.J. 2019 *Plasma Phys. Control. Fusion* **61** 084003
[40] Lin Z.F. *et al* 2020 *Plasma Phys. Control. Fusion* **62** 025025
[41] Tong R.H. *et al* 2019 *Nucl. Fusion* **59** 106027
[42] Jiang Z.H. *et al* 2019 *Phys. Plasmas* **26** 062508
[43] Li C.H. *et al* 2020 *Plasma Phys. Control. Fusion* **62** 095010
[44] Cai N. *et al* 2021 *Fusion Eng. Des.* **169** 112488
[45] Zhang M., Cai N., Yang Y., Zhang J., Zhang Z., Rao B., Chen Z. and Pan Y. 2019 *Fusion Eng. Des.* **146** 1117
[46] Wei Y.N. *et al* 2020 *Plasma Phys. Control. Fusion* **62** 025002
[47] Dai A.J. *et al* 2018 *Plasma Phys. Control. Fusion* **60** 055003
[48] Hu J. *et al* 2020 *Plasma Sci. Technol.* **22** 115102
[49] Li Y. *et al* 2021 *Nucl. Fusion* **61** 126025
[50] Chen Z.Y. *et al* 2016 *Nucl. Fusion* **56** 074001
[51] Lin Z.F. *et al* 2019 *Plasma Phys. Control. Fusion* **61** 024005
[52] Sovinec C.R. *et al* 2004 *J. Comput. Phys.* **195** 355
[53] Shi Y. *et al* 2018 *Nucl. Fusion* **58** 044002
[54] Shi Y. *et al* 2020 *Nucl. Fusion* **60** 064002
[55] Jenko F. 2019 (The GENE development team) The GENE code (http://genecode.org)
[56] Yang Z.J. *et al* 2021 *Nucl. Fusion* **61** 086005
[57] He W., Wang L. and Zhuang G. 2019 *Plasma Phys. Control. Fusion* **61** 115016
[58] Peng S., Wang L. and Pan Y. 2017 *Nucl. Fusion* **57** 036003
[59] Wang L., Peng S. and Diamond P.H. 2018 *Plasma Sci. Technol.* **20** 074004
[60] Huang H. and Wang L. 2020 *Plasma Sci. Technol.* **22** 105101
[61] D'Angelo N. 1965 *Phys. Fluids* **8** 1748
[62] Catto P.J. 1973 *Phys. Fluids* **16** 1719
[63] Guo W., Wang L. and Zhuang G. 2019 *Nucl. Fusion* **59** 076012
[64] Hasegawa A. and Wakatani M. 1987 *Phys. Rev. Lett.* **59** 1581
[65] Guo W., Diamond P.H., Hughes D.W., Wang L. and Ashourvan A. 2019 *Plasma Phys. Control. Fusion* **61** 105002